Chapter 4

MOKE in the Visible-Light Region

4.1 Annealing-induced extension of the helical phase in Tb

Upon cooling many heavy rare-earth (RE) metals attain helical antiferromagnetic order (AF) before they undergo a first-order transition into a ferromagnetic (FM) phase. In Tb metal the AF phase [106] exists only in a very narrow temperature interval between $T_N \approx 230$ K and $T_C \approx 220$ K [7]. The first-order transition at T_C is driven by a gain in magnetostrictive energy that compensates the loss in exchange energy [107]. The resulting changes in lattice volume upon cooling are known to be much larger than ordinary thermal lattice expansion [7]. The magneto-elastic equilibrium that determines the phase transition temperature can be altered through lattice strains, e.g. applied by external forces [108]. In particular a tension equivalent to 680 bar completely suppresses the helical AF phase in a Tb bulk single crystal [109].

Very large *compressive or tensile* lattice strains can easily be achieved through epitaxial growth and numerous experiments on rare-earth multilayers ('superlattices') [110] show the strong influence of *epitaxial strain* on the first-order phase transition [111]. For example in an epitaxially clamped Dy/Lu multilayer system where each layer is a few atomic planes thick, the Dy basal-planes are 2.4 % compressed which reveals a much *higher* T_C [112]. The opposite effect is achieved by a tensile lattice strained Dy in a $[\mathrm{Dy/Y}]_\mathrm{n}$ multilayer where the ferromagnetic phase in Dy is *suppressed* [113]; the same holds for holmium and erbium metal [114, 115]. A recent review of the helical-to-ferromagnetic transition in rare-earth multilayers has been published by Tishin et al. [116].

Comparatively little is known about the stability of magnetic phases in nanometer-thick rare-earth metal films. After the experimental demonstration of excellent heteroepitaxial growth of rare-earth metals on tungsten surfaces [117] most of the experimental studies have been performed on ferromagnetic Gd(0001) on W(110) [101, 118–125]. As in the bulk phase, Gd(0001) films are simple ferromagnets and were found not to exhibit helical order. Investigations on other heavy rare-earth metal films are scarce [39, 126, 127].

In this section are presented studies of the ordering temperature (T_N) and the first-

order phase transition temperature between the helical and ferromagnetic phase (T_C) of 10-nm thick Tb/W(110) with particularmfocus on their dependences on the annealing temperature after deposition of the film. The experimental data were obtained by measuring the magnetic ac-susceptibility with MOKE in the visible-light region. For sensing the ac-susceptibility, an oscillating magnetic field (of 57 Hz and 13 Oe amplitude) was applied to the sample along the b direction of the hcp lattice of Tb metal (parallel to the W(110) direction [128]) which is the easy axis of magnetization [7]. For this purpose a rotatable two-magnet device for magneto-optical studies in UHV [37] was developed and employed. Temperature dependencies were monitored while cooling down the sample at a rate of 1 K/s. Each annealing step lasted for one minute (at a given 'annealing temperature') and was followed by a susceptibility-versus-temperature measurement. Note that annealing was done without moving the sample which assures that all measurements were made on the same spot of the sample; hereby hypothetical substrate inhomogenities can be excluded. The susceptibility-peak position is determined with ± 0.2 K relative accuracy. In the present experiment an absolute temperature calibration was of minor interest. The relative error for comparison of two independent susceptibility curves is ± 0.5 K in the temperature range of data acquisition. The absolute uncertainty of the annealing temperatures is estimated to be ± 5 K. The LEED patterns were recorded *in-situ*. The STM images were taken under the same preparationel and vacuum conditions but in a different experimental chamber[1].

Fig. 4.1 presents ac-susceptibility curves of a 10-nm thick Tb metal film in various annealing steps. The as-grown film (top spectrum) exhibits a double-peaked structure with maxima at 231.5 K and 228.0 K. The two peaks reveal the Neél and Curie temperatures of the film, respectively, reflecting the phase transitions from paramagnetic to helical AF order at T_N and from helical AF to FM at T_C [54, 71]. Successive annealing in increments of 50 K increases the intensity mainly of the second peak. This gain in T_C-peak intensity is accompanied by an increasing temperature difference between the two peaks which is mainly due to a shift of T_C to lower temperatures as indicated by the solid vertical bars in Fig. 4.1. By contrast T_N seems to be rather stationary over the whole annealing temperature range. The largest susceptibility response is obtained upon annealing at 1210 K where the temperature separation between the two peaks amounts to 17.0 K. This is substantially larger than in bulk Tb of which the largest temperature difference reported is 12 K for polycrystalline [54] and 10.8 K for single crystalline Tb [70]. Annealing of the film at even higher temperatures leads to a rapid decrease of the susceptibility signal as is revealed by the lowest two curves in Fig. 4.1.

The most relevant features of the ac-susceptibility curves in Fig. 4.1 are summarized in Fig. 4.2. It clearly reveals that T_N changes only slightly while T_C drops substantially with increasing annealing temperature (cf. Fig. 4.2(a)). There is a pronounced change in slope around 840 K which defines the lower bound of the grey shaded area, in the following referred to as region II. The maximum T_C-peak height (Fig. 4.2(b)) is reached upon annealing at $\sim$ 1200 K which defines the upper bound of region II. At even higher

[1]STM measurements were done in cooperation with M. Bode, Hamburg.

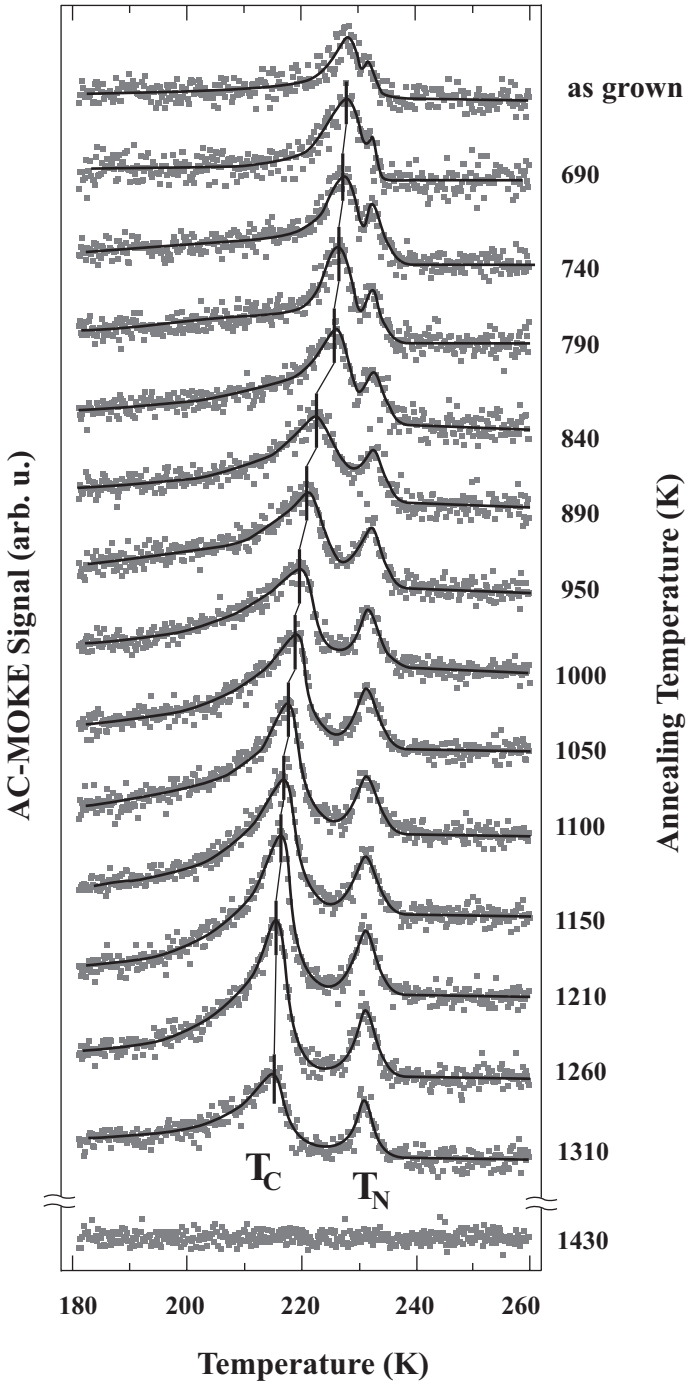

Figure 4.1. ac-susceptibility-versus-temperature curves for a 10-nm Tb/W(110) film upon various annealing steps of 60 s duration at the indicated temperatures (right). At 1430 K the film desorbs completely as indicated by the vanishing susceptibility signal. Amplitude and frequency of the oscillating external field are 13 Oe and 57 Hz, respectively. Vertical bars mark the annealing-induced T_C peak shift. The curves through the data points are guides to the eye.

temperatures (region III) the peak height is strongly reduced, indicating that either most of the Tb film has desorbed or is has broken up into islands. (This interpretation is supported by the appearance of satellite spots in the LEED patterns upon annealing at 1310 K, cf. Fig. 4.4(b); the LEED images will be addressed further below). It is noteworthy that the present Tb films on W(110) when compared with films of the neighboring RE elements in the periodic table, have a remarkable temperature stability. For comparison, the optimum temperature to anneal a Gd(0001) film of the same thickness is much lower (700 K), and it brakes up into islands upon annealing already at some 750 K [118]. Furthermore in Fig. 4.2(b) an obvious change occurs in the T_C-peak height 'annealing characteristics' around 840 K. The height is rather stalled after a rapid increase in region I, but it assumes a steep slope again towards the upper bound of region II. Finally the T_C peak width in Fig. 4.2(c) undergoes pronounced changes *only* in region II.

It has been suggested earlier that the formation of periodic magnetic structures (such as helices) in heavy RE metals is accompanied by the nesting phenomenon of the Fermi surface (FS) (the FS nesting vector quantitatively accounts for the experimentally observed modulation periods [129]). The FS topology depends sensitively on the c/a ratio and does not exhibit nesting above $(c/a)_{crit}$. At this critical value the modulation period approaches infinity, and the magnetic order changes from helical to ferromagnetic (Lifshitz transition) [108,130–132]. The relative stability of helical and ferromagnetic phase depends on a subtle competition between in-plane next-neighbor and interlayer distances [133] – a picture that has been experimentally confirmed for many heavy RE metals in the *bulk* phase [134]. $(c/a)_{crit}$ is practically the same for all heavy RE metals. For bulk Tb metal a value of 1.582 has been given in Ref. [108]. Note that the lattice parameters of *unstrained* bulk Tb ($a = 360.10$ *pm*, $c = 569.36$ *pm* at 20° [135]) corresponds to $(c/a)_{bulk} = 1.5811$ which is barely *below* the critical limit of stable helical order.

There is a large misfit between the bulk lattice parameters of Tb(0001) and W(110) (360.1 pm and 316.5 pm, respectively [135]) which inevitably causes the Tb film lattice to deviate from the bulk case. J. F. van der Merwe used the Peierls-Nabarro (PN) model [136, 137] to discuss the formation of *misfit dislocations* and their *propagation* with increasing film thickness. In this simple model the adsorbed Tb atoms experience only the interaction with the neighboring atoms and the W substrate. The former tends to preserve the natural spacing between the atoms while the latter tends to align them with the substrate. As a result the atoms will be placed at an equilibrium distance of lowest total energy. The main parameter is the misfit η between adjacent Tb layers. For sufficiently large misfits the elastic energy dominates, and dislocations are introduced in the film to lower the elastic energy term. The point of equilibrium between both terms defines the critical misfit η_c.

According to van der Merwe the critical misfit η_c is of the order of 9% for the *first monolayer* that is in direct contact with the substrate. The critical misfit η_c decreases with increasing film thickness and converges to about 3% for *thick* films [136, 137]. According to this model, the huge mismatch between the Tb and W bulk lattice parameters (in the sub-monolayer range) is mastered by reconstruction [138].

Compared with Gd/W(110) films, Tb/W(110) films differ only marginally in bulk lattice constants (Gd: 180 pm vs. Tb: 178 pm [51]), and their growth behaviors in the

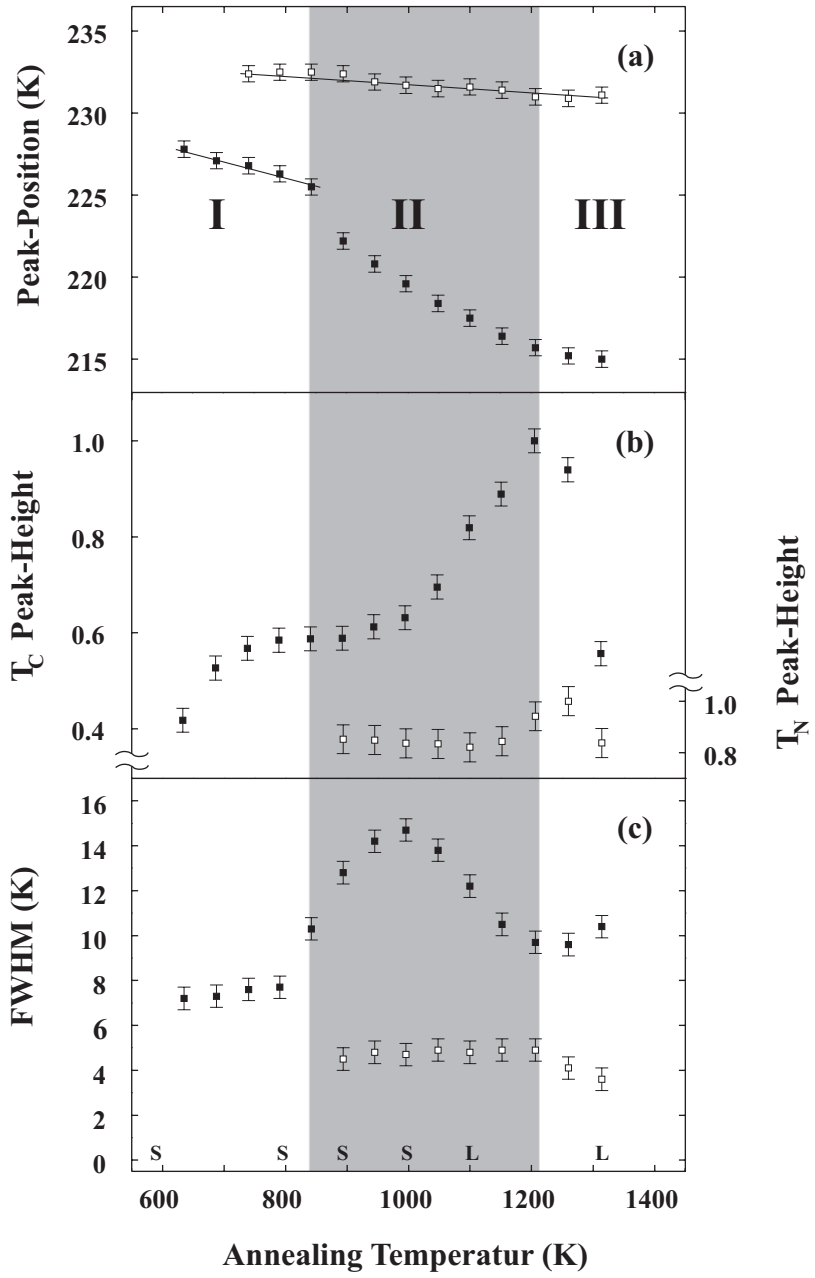

Figure 4.2. Main features of the ac-susceptibility curves presented in Fig. 4.1. (a) Positions of the T_N (upper) and T_C (lower) peak. The average changes in the linear regions (solid lines) are $\Delta T_N/\Delta T_{anneal} = -0.3$ K/100 K and $\Delta T_C/\Delta T_{anneal} = -1.0$ K/100 K. (b) Relative peak heights. (c) Peak widths (FWHM). The grey shaded area indicates the temperature interval (region II) of the most pronounced changes. The letters S and L indicate the annealing temperatures used for the STM images (Fig. 4.3) and for the LEED images (Fig. 4.4), respectively.

sub-monolayer range are known to be almost identical [138]. For a well-annealed first atomic Gd layer on W(110) a 14x7 superstructure has been proposed on the basis of LEED and STM [139], according to which the Gd monolayer is expected to be *expanded* by 1.2% along W[001] and compressed by 0.6% along W[$\bar{1}$10]. Recently an upper bound of the Gd lattice strain of 2% has been reported (with a small relaxation of the tungsten interface layer) [140]. Altogether, a substrate-induced strain of about 1% is realistic for the Gd monolayer on W(110) [141], and it is reasonable to expect the same for the Tb monolayer. The epitaxial strain of 1% is clearly below η_c for thick films so that, according to the van-der-Merwe criterion given above, Tb lattice planes on top of the *presumably reconstructed interface layer* are expected to be strained with respect to bulk Tb metal in a well-annealed film.

How far does the substrate-induced strain extend into the film? It has been experimentally confirmed (and applied in semiconductor design) that film strain decreases *exponentially* with increasing distance from the interface [142, 143]. The exponent $(-2\pi d/p)$ is linear in the distance d from the interface and inverse proportional to the spacing p between dislocations. As a general result of the PN model the strain energy extends over a region of $d \approx \frac{1}{2}p$ from the interface [136, 137]. Thus for small misfits where dislocations have a large spacing it takes many atomic layers of the film for the strain to be released. The Tb film strain of $\sim 1\%$ (see above) is thus expected to extend as far as $\sim$100 nm, an order of magnitude larger than the present film thickness.

From the PN model (above) it is reasonable to assume that the Tb interface layer of a thick film is reconstructed like it is at sub-monolayer coverages. If one assumes about 1% in-plane tensile lattice strain extending throughout the entire film when it is well annealed, and considering anisotropic elasticity (Poisson contraction, continuum linear elasticity) one obtains $(c/a) = 1.556$ that is significantly smaller than $(c/a)_{bulk}$. Within this straight forward estimate[2] the helical magnetic phase should be *more stable in the film* than in bulk Tb metal.

On the basis of van der Merwe's model one arrives at the following conjecture: After deposition at room temperature the Tb film lattice contains many defects. With increasing annealing temperature, the defects and dislocations are expected to be 'expelled from' the Tb film, and the *strained lattice order* increases. Hereby the lattice properties of the film are the more governed by the substrate the better the crystalline order within the film is. It is reasonable to assume that the substrate-induced strains establish a new set of lattice constants for the entire film which do not exist in the Tb bulk crystal. Also one should expect that the system reaches the highest degree of strained crystal order (lowest amount of dislocations in the film) upon annealing at 1210 K, right before substantial desorption.

Fig. 4.3 shows STM images of the surface topography of a 10 nm thick Tb film after different annealing steps. (Same thickness as for ac-susceptibility data in Figs. 4.1 and 4.2.) After gentle annealing at 580 K (Fig. 4.3(a)) islands of several monolayer height dominate the surface topography, and the film looks almost "as grown" at 300 K. Upon annealing at 790 K the film surface has converted to flat terraces (Fig. 4.3(b)). Further

[2]So far the van-der-Merwe growth criterion has been applied to semiconductor systems [144, 145]

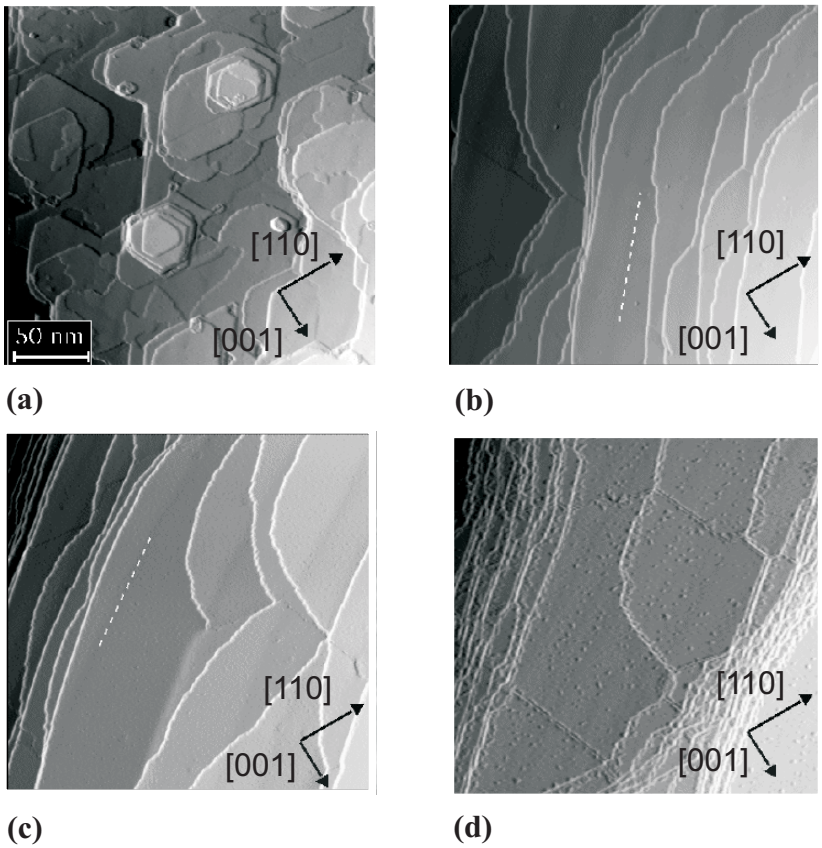

Figure 4.3. STM images of a 10-nm Tb/W(110) film upon annealing at (a) 580 K, (b) 790 K, (c) 890 K, and (d) 1000 K. There is no coincidence between substrate-crystal orientation (arrows) and the step orientation of the film. The steps rather follow the surface steps of the W(110) substrate (cf. white dashed line). The spotty surface in Fig. 4.3(d) is due to technical difficulties in reaching the annealing temperature in the STM apparatus.

annealing at 890 K results in the beginning of surface-step bunching, clearly discernible at the upper left of Fig. 4.3(c). Again higher annealing up to 1000 K gives rise to large terraces (width in the 100-nm range) with a step height of several atomic layers (step bunching), see Fig. 4.3(d). The monotonous behavior of the magnetic susceptibility at temperatures between 1000 K and 1210 K (cf. Figs. 4.1 and 4.2) indicates that there is no further structural rearrangement of the step-bunched Tb surface at higher temperatures until the film finally desorbs.

The LEED image in Fig. 4.4(a) shows the hexagonal Tb(0001) pattern, indicating the presence of a well-ordered hcp lattice of Tb near the film surface upon annealing at 1100 K. (The annealing temperatures used for the LEED images are also given at the bottom of Fig. 4.2.) The absence of satellite reflections in Fig. 4a indicates that the film has not broken up into islands yet. By contrast, after high annealing (1310 K) – upon which the susceptibility peak reduces and widens (cf. Fig. 4.2, region III) – the LEED-pattern is quite different (Fig. 4.4). At least parts of the film have obviously become thin enough to

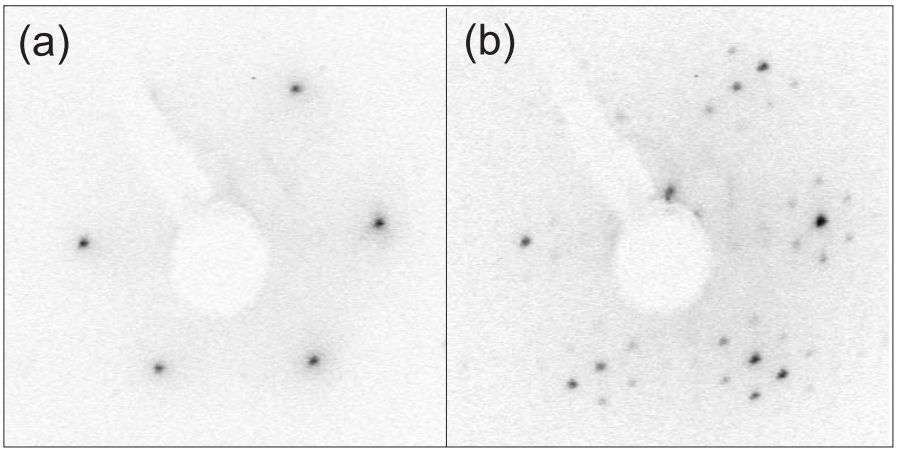

Figure 4.4. LEED patterns (inverted contrast) of a 10-nm Tb/W(110) film recorded at 150 V. Upon annealing (a) at 1100 K there is the characteristic hexagon of hcp Tb. Annealing (b) at 1310 K reveals an interference pattern where satellite spots owe to multiply scattered electrons at substrate- and film atoms. Center and upper left of the images are masked by the electron gun holder.

allow interference with the substrate, and the (partial) brake-up of the film allows one to view the structure of the Tb interface layer. Note that the LEED pattern in Fig. 4.4(b) is virtually identical to those reported for 1 ML Gd/W(110) prepared by thermodesorption at 700 K [140].

Comparing the ac-susceptibility data in Figs. 4.1 and 4.2, show that the T_C-peak initially shifts to lower temperatures in a linear way by $\Delta T_C = -0.3\ K$ for a change of 100 K in annealing temperature. In region II, the T_C peak *position* initially shifts at a steeper slope with a decline to higher temperatures. In region III T_C converges to 215 K. The T_C peak *height* rises until it is stalled at $\sim$ 800 K, and above 1000 K the T_C peak height increases again, reaching a maximum at 1210 K. The T_C peak *width* changes considerably only in region II, reaching a maximum at $\sim$ 1000 K.

The remarkable break from linearity in the T_C peak-position characteristics (Fig. 4.2(a)), at the boundery between region I and II indicates the onset of an enhanced diffusion, taking place once the annealing temperature (the boundery between region I and II is $\sim$ 840 K) has overcome an *effective barrier* of defect mobility in the Tb lattice. From the annealing temperature this barrier can be estimated to 70 ± 5 meV. As the film starts to re-order the new structure nucleates in local domains, and the width of the susceptibility peak increases due to variations in the ordering temperature [146]. This gives evidence for a process of re-arrangement where the temporary loss in lattice order is accompanied by a broader variation of T_C due to the coexistence of strained and unstrained domains. (Note that the width observed here is about 50% smaller than previously observed on a Tb single crystal [70].) The reduction of misfits, however, is probably not so easy in a flat film where the single crystal domains become wider with a decreasing number of dislocations. It is expected that the observed step bunching shown in Fig. 4.3(d) facilitates the reduction of

misfits as the terrace boundaries limit the misfit-free domains.

In summary the observed changes in the magnetic susceptibility coincide with an altered film topography. These observed changes are tentatively attributed to the crystalline structure of the epitaxial Tb film which – upon annealing – gradually adopts the strained Tb lattice parameters of the Tb/W interface atomic plane. Hereby the magneto-elastic equilibrium is modified, and the phase transition from helical to ferromagnetic order occurs at temperatures considerably different from T_C of bulk Tb. In order to support the conjecture – the extended temperature range of helical order is owing to an annealing-induced overall change of the Tb lattice parameters – resonant x-ray scattering experiments at such nanometer-thick Tb films [147, 148] would be helpful.

4.2 Magnetization reversal in Tb films

In the previous section annealing induced shifts in T_N and T_C were presented which show a dependence of the magnetic phase transition on the intrinsic stress. As the sample orders magnetically by cooling down below the ordering temperature (T_N) the magnetic moments are oriented in the easy directions (see subsection 2.4.3). For reversing the magnetization an external field is required in order to overcome the forces which hold the magnetization in the easy direction. The shape of the hysteresis which reflect the one-ion and two-ion contributions to the magnetic ordering, is determined by the field-induced and the remanent magnetization, respectively. They can be quantified to some extent by comparing with the applied external magnetic field.

In this section are presented low-field ($H_{max} = 1$ kOe) magnetization reversal loops from 10-nm Tb/W(110), prepared at various annealing temperatures. Magnetic hysteresis loops were recorded in temperature steps of 2 K between 213 K to 237 K, including bothphase transitions at T_N and T_C.

Hysteresis-loop measurements on 10-nm Tb/W(110), prepared at the usual annealing temperature (890 K) and at high temperature (1150 K) are shown together in Fig. 4.5. By comparing the two data sets in one can observe common features which characterize the general magnetic behavior of Tb near the ordering temperature. The wide shape of the hysteresis between T_N and T_C (where the hysteresis loop becomes reversible) indicates the onset of pure rotation of the magnetic moments from fan to ferromagnetic alignment and thus reflects the enlarged stability of the helix [60, 62]. In the temperature range of helical ordering the sixfold anisotropy of the basal plane is some orders of magnitude smaller compared to the exchange coupling [51, 55, 149] and thus can be neglected. A relevant contribution to the total magnetic energy of the film arises from the two-ion γ-type magnetostriction of which the helical order suppresses the lattice strain (clamped lattice), revealing a contribution only in ferromagnetic alignment [51, 55, 150]. In a hysteresis loop the remanent magnetization is reached after the system has been in a single domain state, and at zero magnetic field γ-strains are known to stabilize the magnetic moments in ferromagnetic alignment [150]. Thus the remanent magnetization can be viewd as a measure for the relative strength of exchange interaction (favoring the helix) and γ-type magne-

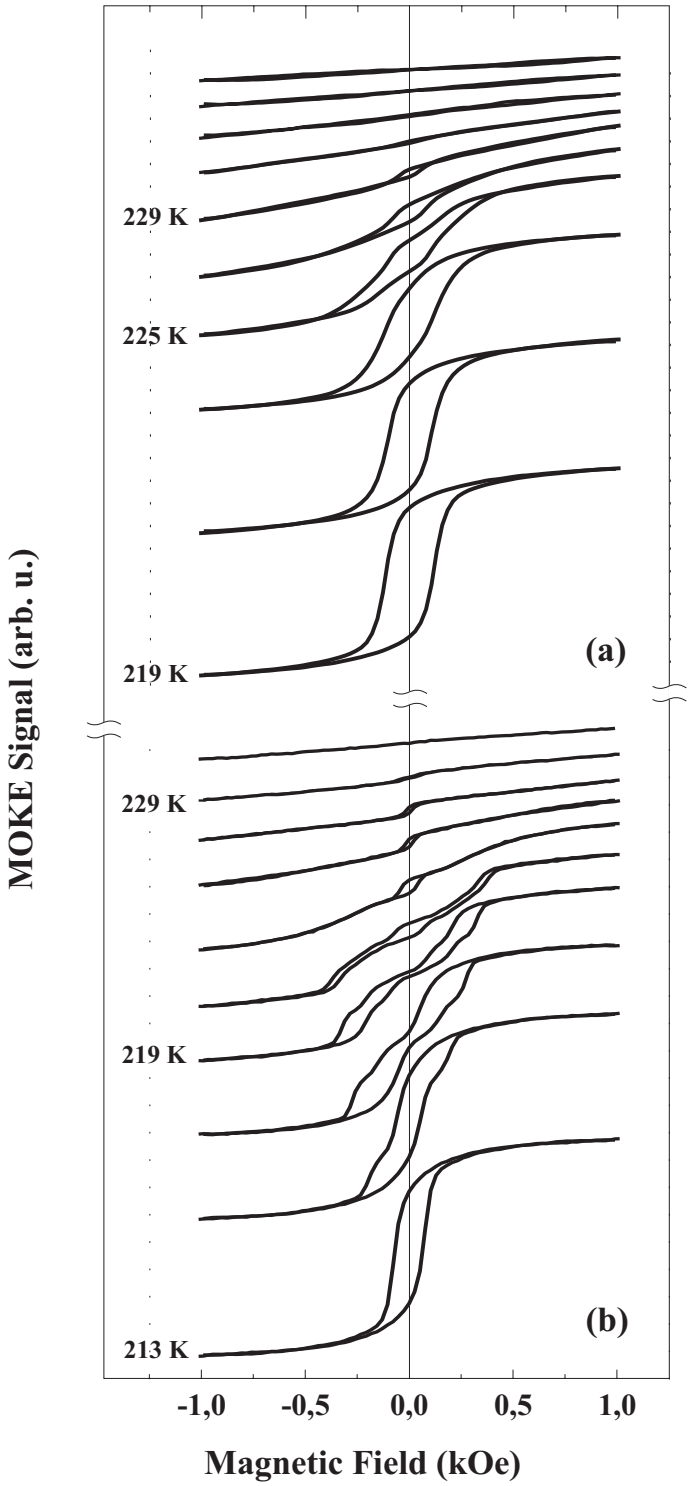

Figure 4.5. Hysteresis loops of 10-nm Tb(0001)/W(110) at various temperatures (in increments of 2 K) between T_N and T_C. (a) Standard preparation of a large-terrace smooth Tb film by annealing at 890 K; (b) after high-temperature annealing (1150 K).

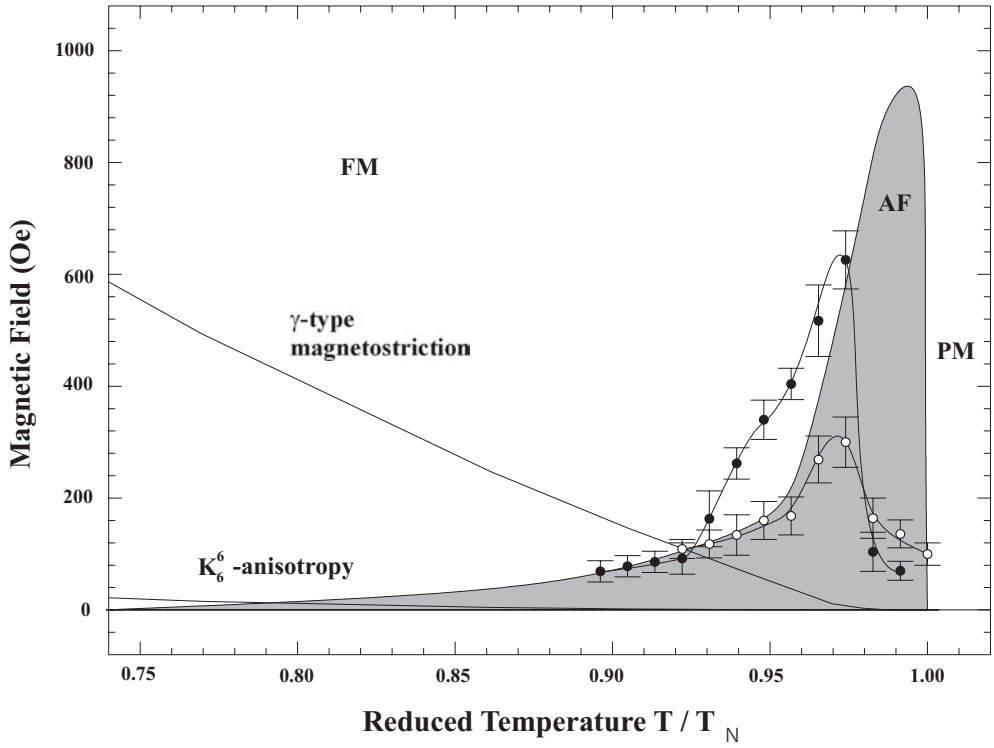

Figure 4.6. Magnetic phase diagram of terbium versus external field. The grey shaded area reproduces the region of stable helical ordering as it is known from literature (see also Appendix). The experimental values are obtained from temperature dependent hysteresis of 10 nm Tb, annealed at 890 K (○) and 1150 K (●). (The curves serve as guide to the eye.) The sixfold in-plane anisotropy K_6^6 (left bottom corner) and the γ-magnetostriction contribution in units of a magnetic field are obtained using theory of Callen & Callen 1966; they are scaled to match experimental data [Feron et al. 1970, Cooper 1967].

tostriction (favoring ferromagnetic alignment). This is meant qualitatively since one never reaches the (thermodynamic) state of lowest energy during a magnetization reversal process at finite speed. As the substrate-induced strain releases with increasing film thickness (section 4.1) the magnetoelastic equilibrium is slightly altered from layer to layer, revealing a gradient in H_{crit} across the film from the substrate/film interface to the vacuum, which leads to a consecutive layer-by-layer switching with increasing magnetic field; this is reflected by the softly ascending flanks of the hysteresis loops.

Although both data sets show similar behavior there are decisive differences regarding their detailed structure. In the low-annealed system (Fig. 4.5(a)) the magnetization shows near T_N a quasi paramagnetic behavior as the weakly coupled spiral undergoes a smooth transition from helix to fan. (Saturation state has not been reached in the present case). Remanent magnetization is first observed at 229 K (opening of a hysteresis loop). In the AF phase (between T_N and T_C) the hysteresis shows small remanence, as it is expected when the helical layer-to-layer coupling is strong. (In a pure helix the net magnetization cancels out.) As the moments are ferromagnetically aligned the γ-type magnetostriction

presumably influence the effect of the external magnetic field. When the field is switched off the magnetostrictive strain partially remains, again preserving a ferromagnetic contribution even in the helical phase (see the small hysteresis loop at zero field, Fig. 4.5(a) at 229 K).

Upon high annealing (1150 K, Fig. 4.5(b)) all features appear to be much more pronounced and the helical phase extends over a larger temperature range (see also section 4.1). The generally smaller coercive fields (Fig. 4.5(b)) show immediately that lattice defects and/or impurities are reduced through annealing. The stability of the helical phase (and also the block phase [61]) is likely to be increased by a strain-induced higher resistance against external fields (Fig. 4.5). (In the present context it is useful to recall that the transition from ferromagnetic to helical order in Tb does not occur abruptly at T_C.) At 219 K where remanence vanishes completely (!), the hysteresis turns into a twin pair of stepped and off-centred satellite loops which may be due to an enhanced stability of the helical phase. As shown by STM scans in section 4.1, there are step bunching effects due to annealing. Thus alternatively there could be a step-induced anisotropy with a large component normal to the bulk crystalline easy axis, similar to a model described by Hyman et al. [78] and others [79, 151]. Actually one cannot distinguish here between the two contributions; probably a combination of both effects leads to the observed field dependence of the magnetization.

To compare the present findings with existing data, the external field at which the helix becomes unstable, H_{crit}, is drawn in a phase diagram. The data from literature [57–61] are represented by the grey-shaded area. The data points of the present work are obtained from the hysteresis loops in Fig. 4.5. As a measure for field stability the points of the strongest curvature in the hysteresis were taken, where the switching from helix to fan is likely to occur. In order not to confuse with the hysteretic effects revealed by the coercive field, the left-hand and right-hand branch of the hysteresis loops where summed up. The results are presented in Fig. 4.6. Experimental data on critical fields H_{crit} span quite a wide range of values up to some 1 kOe [57, 59, 60, 152]. Besides variations in temperature, which just reflect the difficulty to accurately determine T_N (owing to the fact that H_{crit} depends on the sample purity [51]). Low annealing (890 K) is in good agreement with literature and confirms the similarity with Tb bulk properties. At high annealing (1150 K) the stability of the spiral was found to be consistently higher in magnitude. This behavior might be due to the fact that the transition temperatures T_C and T_N and the critical field H_{crit}, needed to deform the helical antiferromagnetic structure, are sensitive to sample purity and previous treatments of the sample. This view becomes particularly plausible when considering the amount of epitaxial strain in the Tb film [60].

4.3 Temperature dependent magnetization of Gd and Tb films

Raw data of MOKE in the visible-light region show a strong temperature dependence of 'non-magnetic' origin [39] which is not surprising since absorption in the visible light involves excitations in the conduction band, i.e. into electronic states that participate in the chemical bonding. Usually one refers to the difference of MOKE data from opposite magnetized samples in order to obtain a signal that is proportional to the magnetization. By contrast squared magnetic dependence is reflected in many solid-state properties, like e.g. elastic moduli [4], electrical and thermal resistivity [2,3], heat capacity [5], sound attenuation [6], and magnetostriction [7]. In this subsection, in order to identify magnetostrictive contributions that influence MOKE signals in the visible-light region, MOKE data from magnetized Gd and Tb films are analyzed with respect to their asymmetric behavior in temperature.

Fig. 4.7(a)-(c) shows the temperature- and field-dependent magnetization of a 10-nm Gd/W(110) film recorded after three different annealing steps. The MOKE signal was measured while cooling the sample in a external field of $H_{ext} = 40$ Oe (solid) and 800 Oe (open circles), which were applied along the easy axis of magnetization. The magnetic contrast is obtained by recording the MOKE signal twice, with the magnetic field along opposite directions. The difference of the MOKE curves ($I^+ - I^-$, named "diff.") is shown together with the corresponding raw data ("raw") which are displayed directly above.

As described in Sect. 3.2, the difference of the MOKE signals is proportional to the sample magnetization. In the difference depicted in Fig. 4.7(a)-(c) one observes the onset of the magnetization at Gd bulk $T_C = 289$ K [153] with a steady increase in magnitude to lower temperatures. Remarkably the magnetization starts with a steep increase which turns over into an almost linear rise not far below T_C. One also observes that the magnetization increases when a higher magnetic field is applied to the sample. This field induced rise of the magnetization is almost constant ($\sim$ 15%) over the whole experimental temperature range of ferromagnetic order. This behavior is in good agreement with single crystalline bulk Gd [153].

Fig. 4.8 displays temperature- and field-dependent magnetization curves of 10-nm Tb/W(110) films after different annealing steps. While the difference of the MOKE signals shows the characteristic temperature dependence of the Tb bulk magnetization [71], one imediately observes that the raw MOKE data contain significantly larger contributions 'non-magnetic' origin than similar curves from Gd (Fig. 4.7). Below the ordering temperature T_N the signal starts to 'bend away' from the extrapolated linear paramagnetic behavior (dashed line). The strongest curvature is achieved upon high-temperature annealing (at 1210 K, cf. Fig. 4.8(c)). Moreover, the influence of the applied magnetic field on the magnetization is considerably stronger in the case of Tb than in Gd (cf. Fig. 4.7). This observation can be understood by the help of Fig. 4.6 that shows the stability of the helical phase in Tb (section 4.2). As the Tb film is cooled down in an external field of 800 Oe – which is high enough to overcome helical order – the magnetic moments will be

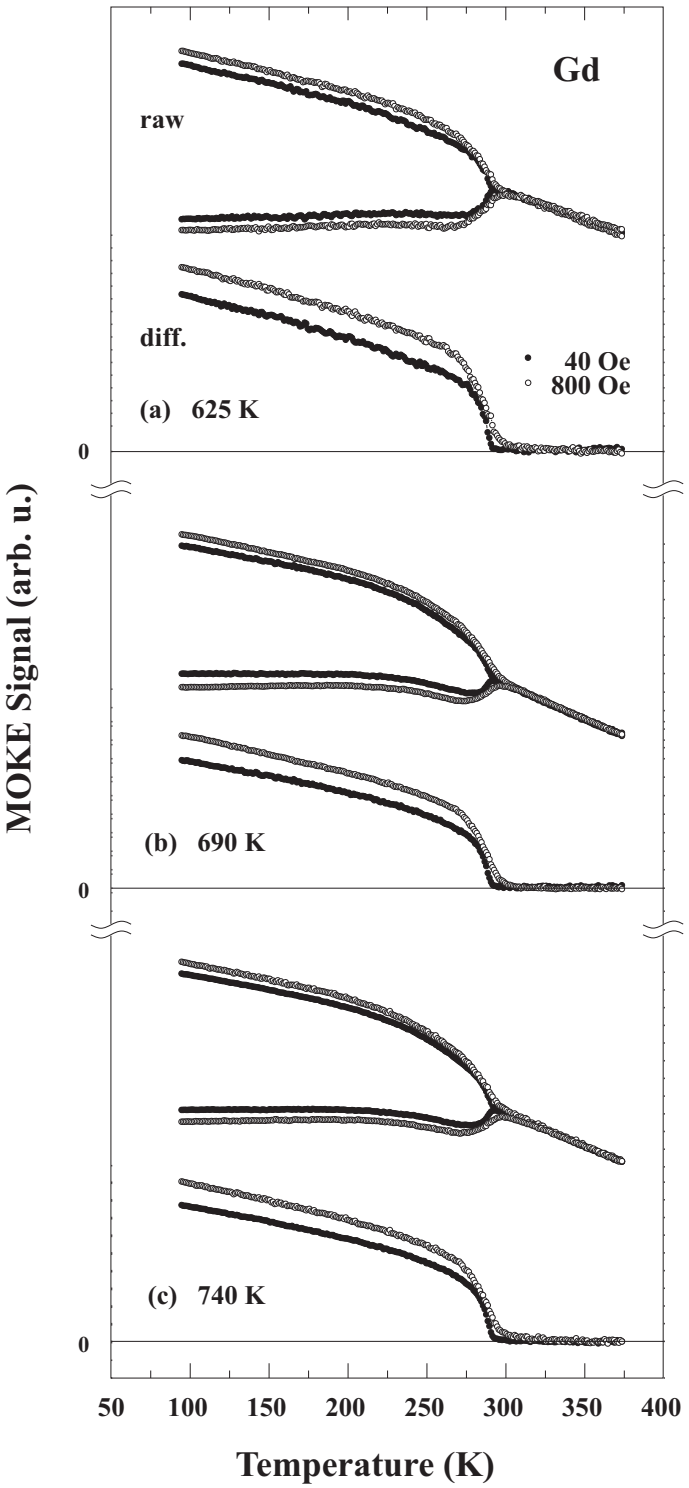

Figure 4.7. Visible-light MOKE signal of 10-nm Gd/W(110), annealed at 625 K (a), 690 K (b), and 740 K (c), recorded while cooling down the samples in an external field of 40 Oe (•) and 800 Oe (◦). Below T_C the raw data curves split into an upper and a lower branch indicating opposite sample magnetization. External fields were applied along the hcp-crystal b axis (easy axis of magnetization in bulk Gd metal).

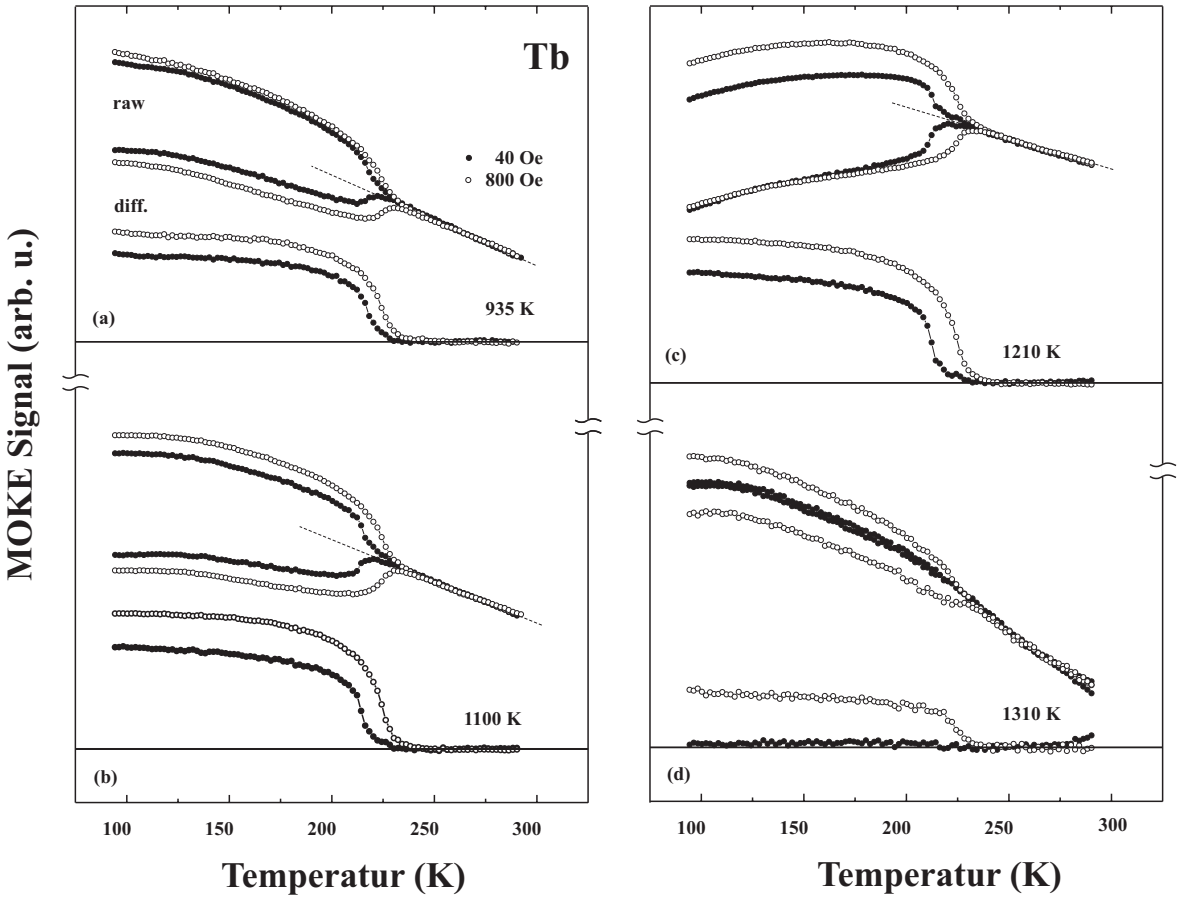

Figure 4.8. Visible-light MOKE signal of 10-nm Tb/W(110), annealed at 935 K (a), 1100 K (b), 1210 K (c), and 1310 K (d), while cooling down in a external field of 40 Oe (•) and 800 Oe (○).

given a preferential alignement in field direction at all temperatures. By contrast, 40 Oe is far below H_{crit} necessary to overcome the helical exchange coupling $[\mathcal{J}(Q) - \mathcal{J}(0)]$, i.e. to 'break' helical order (see section 2.4). Hence it is reasonable to assume that at 40 Oe a helical state is established right below T_N, which usually leads to a heli-fan around T_C [63]. Contrary to the fan the heli-fan includes complete rotations of the basal plane magnetization about the c-axis, hence it cannot be transformed into a ferromagnetic structure (that is free of such rotations). The substantially reduced magnetization of the Tb film in the 40-Oe field curves (Fig. **??** is thus attributed to the presence of heli-fan structures, which upon cooling (to some 100 K) lead to the presence of 360° walls that reduce the net magnetization in the ferromagnetic phase.

The sum of the MOKE signals ($I^+ + I^-$) should reflect only these contributions which have a symmetric behavior upon magnetization reversal, i.e. which go with even powers of the magnetization, $I^+ + I^- = F(M^2, M^4, \ldots)$. The sum of the MOKE signals from Gd is shown in Fig. 4.9(a)-(c). In 4.9(a) one can distinguish two regions of approximately linear behavior with pronounced kinks in between them. There is one at 228 K and one near

T_C. (It could also be one broad transition around ~ 256 K.) As the annealing temperature is increased from 625 K to 690 K, the two kinks merge indicating *one* smooth transition that extends from 200 K to 240 K, separating two linear regions with different slopes. Annealing at 740 K does not induce any further changes. The significant change in the first annealing step might reflect the brake-up of the Gd film into islands, which has indeed been observed for such films [146]. Yet it is quite unlikely to happen at such a low temperature ($625 < T < 690$ K), since in a study of the annealing properties of Gd/W(110) by ac-susceptibility (similar to section 4.1) it was found that 740 K is the optimum annealing temperature (at which the T_C susceptibility peak becomes most pronounced). Also the improved signal-to-noise ratio of the data for 690 K and 740 K annealing is reminiscent of a flat film that has not broken up into islands. The applied field has no significant influence; this is expected since in Gd metal there is no exchange contribution to the magnetostriction (section 2.4.4) and hence no 'forced magnetostriction'.

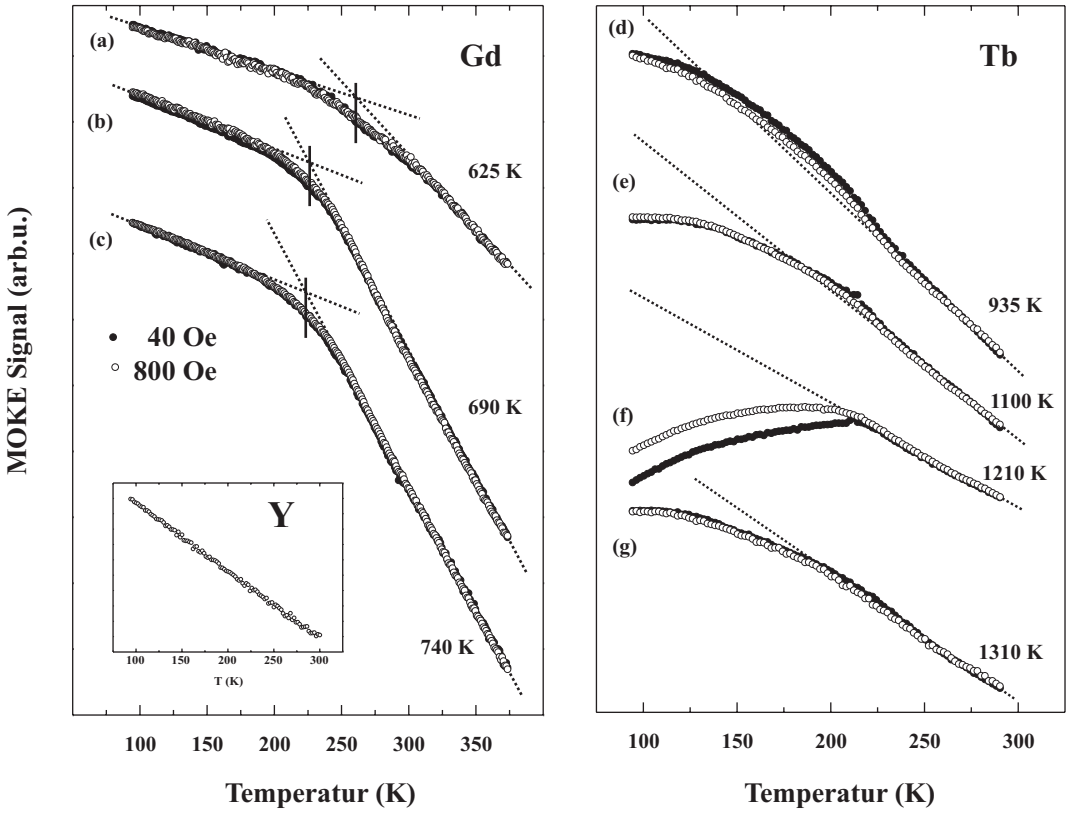

Figure 4.9. The sum of the visible-light MOKE signal for both magnetizations of (left) Gd/W(110), annealed at 625 K (a), 690 K (b) and 740 K (c), and (right) Tb, annealed at 935 K (d), 1100 K (e), 1210 K (f) and 1310 K (g). The Gd data show a kink which is located at 256 K (a) and 228 K in (b) and (c), respectively. In (d) to (g) a dotted line shows the extrapolated linear behavior of the paramagnetic region. The inset shows the reflectivity of a non-magnetic yttrium metal film in the same temperature range.

It is a well-known magnetic property of bulk Gd that the magnetic moments undergo

a reorientation (spin reorientation, SRO) at $\sim$ 226 K [122, 154]. Above 226 K bulk Gd moments are parallel to the c axis, below they start to tilt away from the c-axis reaching a maximum angle of about 70° (w.r.t. the c axis) around 195 K; it reduces again to $\sim$ 30° at 4.2 K [55]. This behavior is reflected in the lowest-order anisotropy constant K_2 which changes sign at T_{SRO}. At this temperature many macroscopic magnetic, thermal, and electrical properties of Gd show anomalies, including magnetization [152, 153], magnetostriction [155], thermal expansion [156], elastic constants [157], electric resistance [3], and magneto-resistance [158].

In thin films (nm-range) the magnetization is forced to lie in the film plane due to the dominating magnetostatic energy $\propto M^2$, and the threshold for an out-of-plane magnetization is simply given by the ratio between the uniaxial anisotropy constant and the magnetostatic energy [122]. Due to a different dependences of the crystalline anisotropy and the magnetostatic energy on film thickness, the SRO-transition temperature depends also on the film thickness [122]. There is a critical thickness ($\sim$ 30 nm) below which the magnetostatic energy gains over the bulk crystalline K_2 anisotropy, that favours an out-of-plane magnetization above T_{SRO}. With increasing thickness, the transition temperature drops off and levels at a certain temperature for thick films ($\sim$ 100 nm), i.e. becomes independent of the thickness [122].

The inability to completely anneal strains in thin Gd films gave rise to the suggestion that the first few nm of Gd/W(110) are still under substrate-induced strain and have not developed bulk anisotropies [154]. In accordance with the observations reported in section 4.1 for Tb, it appears natural that substrate-induced strains can alter the balance between anisotropy and magnetostatic energy, which determines T_{SRO}.

The crystalline anisotropy of the present 10-nm thick Gd/W(110) films, although not strong enough to pull the magnetization out-of-plane, has still a minimum at T_{SRO} where $K_2 = 0$. The observed kink at 228 K, cf. Fig. 4.9 (b) and (c), is in excellent agreement with literature values of T_{SRO} in bulk Gd [122, 154]. This shows that the well known anisotropy minimum in Gd is obviously accompanied by a (magnetostrictive) response of the lattice, which is an interesting observation that could be subject of further investigations of the temperature dependent Gd lattice constants, e.g. by x-ray structure analysis.

The linear change in light intensity, as it is shown in Fig. 4.9 in the paramagnetic region, cannot be of magnetic nature and rather reflects the usual thermal lattice contraction. Recalling eq. 3.7 (section 3.2) the sum signal, recorded in the present experimental setup is proportional to reflectivites of s- and p-light and the sinus of their relative phase Δ:

$$\left(I^+ + I^-\right) \propto r_p r_s \sin\Delta \cos\alpha\,. \tag{4.1}$$

The paramagnetic change in the light intensity is supposed to go with a change in the phase between r_s and r_p ($\sin\Delta$), although in principle it could also be a change in the overall light intensity ($r_s r_p$) due to a temperature dependence of the bandstructure. (The cosine of α expresses the relative orientation of polarizer and analyzer and therefore is constant.) However, sliding the analyzer from near-extinction ($< 90°$) to opposite near-extinction ($> 90°$) changes the sign of the temperature dependent MOKE signal, i.e. the changes

are phase sensitive! From this one may conclude that the normal lattice contraction is reflected in the phase between the s- and p-contributions of the MOKE signal.

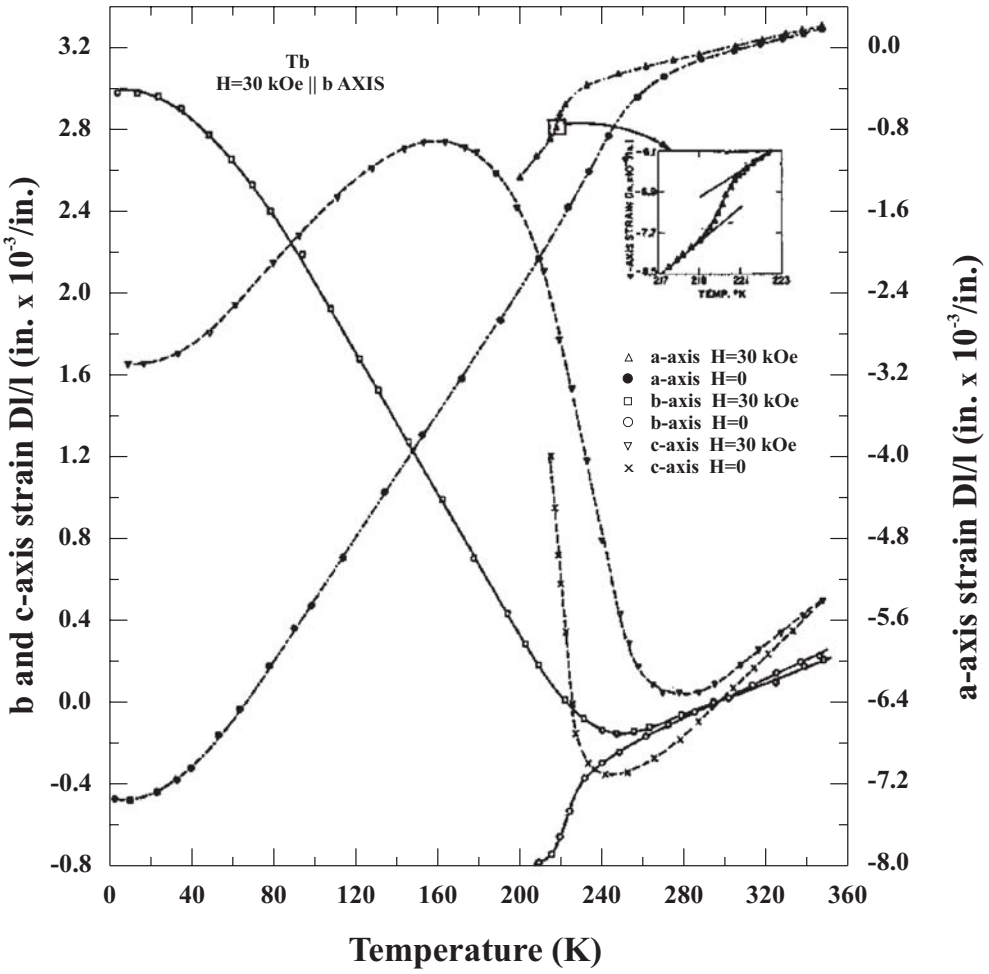

Figure 4.10. The a-, b-, and c-lattice strains of bulk Tb metal as a function of temperature for both, 0 and 30 kOe applied field along the b-axis. The inset shows the anomalous slope change of the a-axis zero field strain around 220 K, which corresponds to a structure change from hexagonal to orthorhombic at the ordering temperature, from [Rhyne & Levold 1965].

It seems reasonable to separate magnetic and other thermal contributions by extrapolation of the paramagnetic behavior to low temperatures [92]. Alternatively, the magnetic contribution may be obtained by comparing with the behavior of a non-magnetic element with comparable electron configuration. This is a common procedure which has been applied successfully in determining, e.g., the magnetic part of the heat capacity in rare-earth metals [5, 50]. Here yttrium was chosen as non-magnetic counterpart since it crystallizes in the same hcp structure as Gd and Tb and its lattice parameters are almost identical [135]. The temperature dependence of the MOKE signal of yttrium is shown in the inset of Fig. 4.9. Its surprisingly linear behavior clearly justifies the strategy of extrapolat-

ing the paramagnetic lattice contraction in Gd and Tb down to low temperatures, which is qualitatively accentuated by the dashed lines in Fig. 4.9.

The MOKE sum signal of Tb is presented in Fig. 4.9(d)-(g). Besides the overall linear temperature dependence, the Tb sum shows the onset of a curvature in the vicinity of the ordering temperature. Upon annealing at 935 K the curvature starts approximately at T_N, first increasing and then decreasing the slope, after having changed the sign at T_C. At higher annealing temperatures the curvature becomes more pronounced, and the largest deviation from a linear (paramagnetic) behavior is reached upon annealing at 1210 K. This is in coincidence with the largest susceptibility peak height (cf. section 4.1) and the most stable helical phase. Also one observes that the curvature now starts only at T_C and immediately decreases the overall slope of the curve.

In contrast to Gd, where the MOKE sum is indifferent upon the applied magnetic field (Fig. 4.9(a)-(c)), Tb shows a strong field dependence. As for the curvature of the sum, the maximum difference between low field (40 Oe) and high field (800 Oe) is obtained upon annealing at 1210 K. Taking the linear extrapolated paramagnetic temperature dependence as being the primer developement of the sum, the anomal lattice expansion (magnetostriction) which sets in below the ordering temperature, may be classified as follows: It either enforces (steeper slope) or weakens (flatter slope) the effect of the normal lattice contraction. The same criterion may be applied for the magnetic field dependence. In this context note the interesting detail, that the field effect reverses its sign from 935 K to 1210 k annealing temperature, i.e. after annealing at 935 K the external field weakens the deviation from paramagnetic behavior whereas at 1210 K annealing the field enforces it.

Fig. 4.10 shows the temperature dependence of a, b, and c strains in bulk Tb as a function of the applied magnetic field along the b-direction (taken from [159]). Clearly one can observe the onset of the anomal lattice expansion below T_N in all directions (a, b, and c). However, there are two outstanding characteristics which distinguish the a-, b-, and c-contributions by their behavior: (1) the applied field enforces or weakens the effect, and (2) the anormal lattice expansion goes in the same or in the opposite direction of the normal lattice contraction. With this the a, b, and c strains (Fig. 4.10) may be characterized as: In *a-direction* (1) weakens and (2) is in the same direction. In *c-direction* (1) enforces and (2) is in the opposite direction. Finally in the *b-direction* (1) is undefined because (2) changes sign (!). The onset of the anomalous lattice contraction in b-, and c-direction is around the ordering temperature. Only in a-direction the onset of anomalous contraction occurs at a surprisingly high temperature of ~ 270 K.

Comparing with the measured data one finds that the anomalies observed after annealing at 935 K show characteristic features of the a-magnetostriction (at least in the vicinity of the ordering temperature), whereas upon annealing at 1210 K the data clearly reveal characteristic features of c-magnetostriction. Therefore in the low temperature annealed system the MOKE signal from the relative change in volume $\Delta V/V$ rather reflects the a-direction which is related to changes of the γ-type (see section 2.4.4). Intuitively this is in agreement with a high number of misfit dislocations and the resulting elevated coercive fields (section 4.2). Analogously, in the high-annealed system the $\Delta V/V$ reflects rather the c-direction which is related to the α-type strains (The α-type strains change the c/a ratio and thus affect phase transition [108]), going with the extended helical phase reported in section 4.1.